Study on Starting Characteristics of Slotted Disc Magnetic Coupler under Graded Starting

Chaojun Yang, Yuan Gao, Jian Wang

Abstract—**The startup challenges of magnetic couplers operating under high-speed slip and heavy-load conditions are studied in this research. An equivalent magnetic circuit (EMC) model is developed to analyze the electromagnetic torque characteristics and enable a graded soft-start performance in a slotted disc magnetic coupler. The electromagnetic torque formula is derived by integrating the EMC method with Ampère's circuital law and Kirchhoff's current law. A kinematic analysis under loaded conditions is then used to establish a system dynamic response model, examining transient startup behavior. Finite element analysis (FEA) simulations generate torque-speed curves for varying input speeds, providing insights into no-load and load-starting characteristics. To address startup failures caused by insufficient locked-rotor torque, a graded soft-start strategy is proposed. This strategy progressively increases input speed to enhance critical torque and overcome load torque, resulting in a significant reduction in startup failures. The accuracy and reliability of the proposed transient theoretical and FEA models are confirmed by experimental validation, with observed deviations within acceptable tolerances. These findings provide a robust framework for the initial design phase of magnetic couplers, for enhanced startup performance under high-speed slip and heavy-load conditions.**

Index Terms—**Slotted disc magnetic coupler, magnetic circuit method, mechanical characteristics, graded soft-start method， electromagnetic torque.**

I. Introduction

The magnetic couplers offer contactless power transmission through magnetic interaction between conductor and permanent magnet (PM) disks, eliminating mechanical wear and lubrication needs. Their advantages have led to extensive research and widespread applications [1-6]. While many studies analyze magnetic field and torque performance using simplified two-dimensional models [7-9], these often require intensive calculations due to the structural complexity of magnetic couplers. More comprehensive theoretical models, such as the vector magnetic potential method [10-12] and equivalent magnetic circuit (EMC) method [13-17], have been developed to account for structural configuration and material properties, improving accuracy. Slotted magnetic couplers, in particular, offer enhanced torque density and reduced eddy current losses due to the flux-concentrating effect of their tooth-slot structures, further improving operational efficiency [18-20].

However, current research predominantly focuses on improving the precision of steady-state torque and magnetic field calculations. Limited attention has been paid to the transient dynamic performance of magnetic couplers [21-23], especially during startup under the demanding conditions of high-speed slip and heavy loads encountered in practical applications. In marine and mining industries, where magnetic couplers are frequently required to start under high-speed conditions, frequent slip can occur. Understanding the transient startup characteristics and load capacity of magnetic couplers during these transmission processes is therefore critical to ensuring reliability and efficiency in real-world scenarios. Specifically, startup failures due to insufficient locked-rotor torque remain a significant challenge.

To address the challenge on the slotted disk type magnetic coupler, an analytical model based on equivalent magnetic circuit theory is developed to characterize electromagnetic torque under variable air gap. Additionally, a transient dynamic analysis of the magnetic coupler is conducted, and a system dynamic response model is developed to investigate startup characteristics. Two operational scenarios—no-load and loaded conditions—are systematically investigated, analyzing cases where the critical torque exceeds or falls below the locked-rotor torque to ensure reliable startup operations. A graded soft-start strategy designed for high-speed and heavy-load operations is proposed and validated, with particular emphasis on the analysis, simulation, and experimental testing of startup characteristics. Unlike previous studies that primarily focus on steady-state analysis, this paper provides a comprehensive transient dynamic analysis and proposes a practical soft-start strategy for reliable startup under high-speed and heavy-load conditions. The results demonstrate the effectiveness of the proposed method in achieving reliable startup under such challenging operating conditions.

II. Basic Structure and Working Principle

The slotted disk magnetic coupler, as illustrated in Figure 1, comprises two primary components: a PM rotor (Figure 1a) and a conductor rotor (Figure 1b). The PM rotor consists of 18 permanent magnets (PMs) and a PM back iron. The PMs are arranged in an alternating N-S pole configuration on the back iron surface, generating a specific magnetic field distribution. The conductor rotor includes a

Manuscript received April 7, 2025; revised August 6, 2025.

This work was supported in part by the State Key Laboratory of Mechanical Transmission for Advanced Equipment Open Fund under Grant SKLMT-MSKFKT-202331.

Chaojun Yang is a professor in the School of Mechanical Engineering at Jiangsu University, Zhenjiang Jiangsu, 212013, China (corresponding author to provide email: yangchaojun@ujs.edu.cn).

Yuan Gao is a master's student in the School of Mechanical Engineering at Jiangsu University, Zhenjiang Jiangsu, 212013, China (email: 15192811889@163.com).

Jian Wang is a master's student in the School of Mechanical Engineering at Jiangsu University, Zhenjiang Jiangsu, 212013, China (email: 1831902253@qq.com).

copper-based conductor disk embedded with 16 fan-shaped iron teeth uniformly distributed circumferentially, along with a conductor back iron.

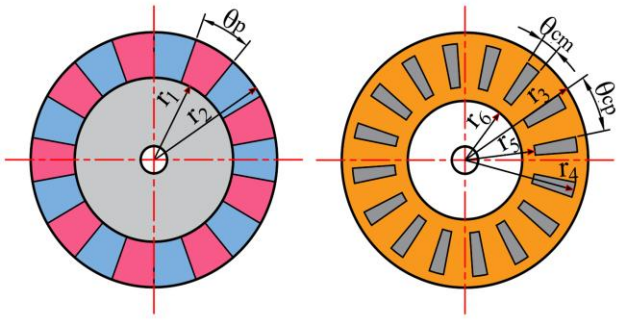

(a) PM rotor (b) Conductor rotor

Figure 1. Model of the slotted disk magnetic coupler.

During operation, the motor drives the PM rotor, creating a speed difference (slip) between the PM rotor and the slotted conductor rotor. Based on the principle of electromagnetic induction, eddy currents are induced in the copper conductor. The magnetic field generated by these induced eddy currents interacts with the magnetic field produced by the PMs, driving the conductor rotor and enabling torque transmission. The material parameters of the PMs, yoke iron, and copper disk are listed in Table I. The structural parameters of the PM disk and slotted conductor disk are provided in Table II.

TABLE I
Material properties of the magnetic coupler.

Parameter	Value
Relative permeability of PMs, μ_r	1.099
Coercive force of the PMs,H_{cb}	876kA/m
Relative permeability of back iron,μ_b	8000
Conductivity of the back iron,σ_b	2×10^6S/m
Permeability of vacuum, μ_0	$4\pi\times10^{-7}$H/m
Conductivity of the conductor,σ_{cu}	5.71×10^7S/m

TABLE II
Structural parameters of the magnetic coupler.

Parameter	Value
Number of PM pole pairs, p	9
Angle of pole pitch, θ_p	20°
Outer radius of the PMs, r_1	125mm
Inner radius of the PMs, r_2	80mm
Thickness of the PMs, t_m	10mm
Thickness of the PM back iron,t_{mb}	10mm
Angle of slot, θ_{cm}	7.5°
Angle of slot pitch, θ_{cp}	22.5°
Outside radius of the CS, r_3	140mm
Outer radius of slots, r_4	125mm
Inner radius of slots, r_5	80mm
Inner radius of conductor, r_6	75mm
Thickness of the CS, t_c	10mm
Thickness of the CS back iron, t_{cb}	10mm

III. Electromagnetic Torque Calculation

A. *Establishment of the Equivalent Magnetic Circuit Model*

To facilitate the analysis by converting the magnetic field into an equivalent magnetic circuit, the following assumptions are made:

1) The primary magnetic flux passes perpendicularly through the PM rotor, the air gap, and the copper conductor rotor.

2) The influence of external conditions on material properties is neglected. The material properties of each component in the magnetic circuit are assumed to remain constant, and material losses are not considered.

3) The axial thickness of the yoke iron is sufficiently large that magnetic saturation effects are negligible. This assumption is valid because the yoke iron is designed with a large cross-sectional area to minimize flux density.

4) The relative permeability of the PMs, copper conductor, and air is assumed to be unity.

The model's accuracy is limited by the simplifying assumptions made, particularly the neglect of material losses and magnetic saturation. These limitations should be considered when interpreting the results.

To simplify the analysis, the three-dimensional magnetic coupler is expanded along the mean radius （$r_m=r_1+r_2/2$) in the circumferential direction, transforming it into a two-dimensional model. This simplification significantly reduces the computational complexity of the analysis while still capturing the essential magnetic field behavior. Figure 2 illustrates the magnetic flux paths after this circumferential expansion. Due to the slotted conductor disk and the relative position changes between the PM disk and the slotted conductor disk, the specific distribution of the magnetic field varies. As shown in Figure 2, Loop 4 represents a simplified flux path where the main flux path corresponding to the S-pole passes primarily through the copper conductor, while the main flux path corresponding to the N-pole passes primarily through the tooth-slot yoke iron. Conversely, Loop 3 represents a more complex flux distribution, where the main flux paths corresponding to both the N-pole and S-pole simultaneously pass through both the copper conductor and the tooth-slot yoke iron.

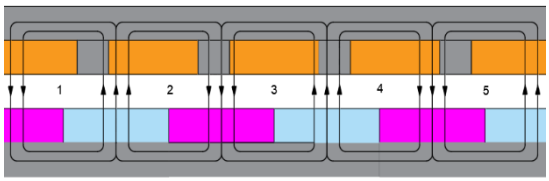

Figure 2. Magnetic circuit distribution of the magnetic coupler.

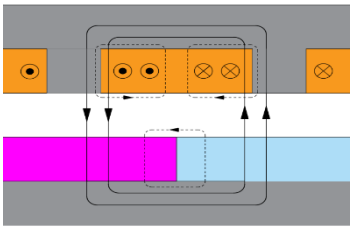

Figure 3. Magnetic flux path of the magnetic coupler.

Although the magnetic flux paths vary among different loops, all loops can be represented using the magnetic circuit of Loop 3. Therefore, this paper selects the more complex Loop 3 as the subject for analysis and constructs an equivalent magnetic circuit model. Prior to establishing this model, the leakage flux and induced flux paths are analyzed, as shown in Figure 3. In this figure, solid lines represent the main flux paths, while dashed lines denote the leakage flux and induced flux of the PMs. Based on the magnetic circuit analysis in Figure 3, the equivalent magnetic circuit model corresponding to Loop 3 is constructed, as illustrated in Figure 4. Due to the numerous branches and complexity in

Figure 4, the model is further simplified, and the resulting simplified equivalent magnetic circuit model is presented in Figure 5.

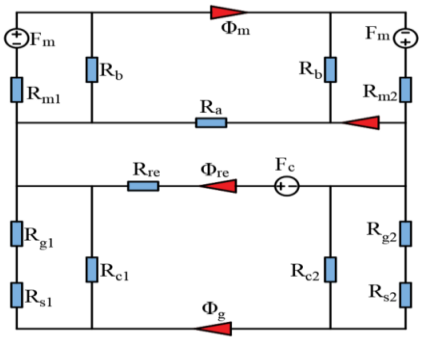

Figure 4. Magnetic flux path of the magnetic coupler.

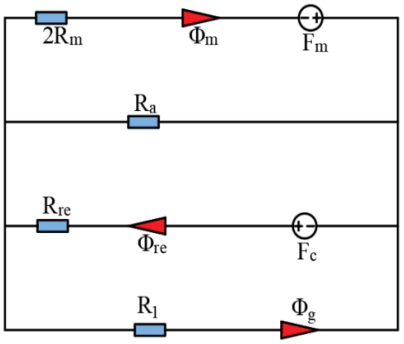

Figure 5.Simplified equivalent magnetic circuit model

In Figure 4, the expression for the magnetomotive force F_m of the permanent magnet is given by[16]:

$$F_m = H_a t_m \tag{1}$$

where H_a is the coercivity of the permanent magnet，t_m is the thickness of the permanent magnet.

The expression for the magnetic reluctance of the permanent magnet is:

$$R_m = \frac{2t_m}{\mu_0 \mu_1 \tau_m w_p} \tag{2}$$

where μ_0 is the permeability of vacuum，μ_1 is the relative permeability of the permanent magnet,，τ_m is the average circumferential length of the permanent magnet, given by $\tau_m=r_m \cdot \theta_m$; w_p is the average radial length of the permanent magnet, taken as $w_p=r_2-r_1$.

The air gap magnetic reluctance corresponding to the slot yoke between the teeth and the permanent magnet is:

$$R_{g1} = \frac{l_g}{\mu_0 \tau_{i1} w_p}, R_{g2} = \frac{l_g}{\mu_0 \tau_{i2} w_p} \tag{3}$$

The relative permeability of the copper conductor is nearly equivalent to that of air. Thus, the magnetic reluctance of the copper conductor corresponding to the permanent magnet and the air gap is expressed as:

$$R_{c1} = \frac{l_g + t_c}{\mu_0 \tau_{c1} w_p}, R_{c2} = \frac{l_g + t_c}{\mu_0 \tau_{c2} w_p} \tag{4}$$

where l_g is the air gap thickness, t_c is the copper disk thickness, τ_{i1} and τ_{i2}, are the average arc lengths of the yoke teeth opposite the permanent magnet, τ_{c1} and τ_{c2} are the average arc lengths of the copper conductor opposite the permanent magnet.

The magnetic reluctances of the yoke teeth are given by:

$$R_{s1} = \frac{t_c}{\mu_0 \mu_2 \tau_{i1} (r_2 - r_1)}, R_{s2} = \frac{t_c}{\mu_0 \mu_2 \tau_{i2} (r_2 - r_1)} \tag{5}$$

The leakage flux between adjacent permanent magnets is described as:

$$R_a = 1 / \int_0^{r_a} \frac{\mu_0 w_p dr}{\pi r} \tag{6}$$

$$r_a = \min\left\{1_g + t_c, \tau_m / 2\right\} \tag{7}$$

Due to the tightly arranged configuration of the permanent magnets, the unilateral leakage flux is negligible, and R_b is disregarded.

The total magnetic reluctance in the simplified circuit is:

$$R_l = (R_{g1} + R_{s1}) // R_{c1} + (R_{g2} + R_{s2}) // R_{c2} \tag{8}$$

B. Eddy Current Effect Calculation

Due to the opposing orientations of the copper conductor relative to the PM's N-pole and S-pole, the induced current direction changes accordingly. During magnetic coupler operation, the induced current distribution varies across different loops, leading to differing formulas for the induced magnetic field. However, the calculation process remains fundamentally similar. Loop 3 is taken as an example to calculate the induced magnetic field, and a coordinate system is established for this calculation, as shown in Figure 6.The expression for the initial magnetic flux density passing through the air gap is[17]:

$$B_{av} = \frac{2\phi_g}{w_p \tau_m} \tag{9}$$

where Φ_g is the air gap magnetic flux.

The radial average induced eddy current density in the copper conductor is further derived as:

$$J_{av} = \sigma_c \nu B_{av} = \frac{\sigma_c \pi n_2 B_{av} r_m}{30} \tag{10}$$

where σ_c is the electrical conductivity of the copper conductor, the speed difference between the permanent magnet disk and the conductor disk, $n_2=n_1-n_0$.

The magnetomotive force (MMF) generated by the eddy currents in the conductor disk is expressed as:

$$F_c = \int_v J \cdot dS = J_{av}\left[(\tau_{c1} + \tau_{c2}) t_c\right] = \frac{\sigma_c \pi n_2 B_{av} r_m (\tau_{c1} + \tau_{c2}) t_c \phi_g}{15 w_p \tau_m} \tag{11}$$

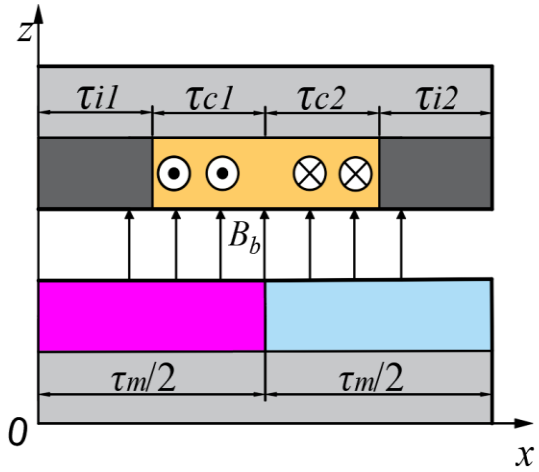

Figure 6. Coordinate system for induced magnetic field calculation

In the region $0 \leqslant x < \tau_{i1}$, the reaction magnetic flux is generated by the superposition of the induced eddy currents in the copper conductor corresponding to the permanent magnet in loop 2 on the left side and the permanent magnets in loops 3 on the right side. According to Ampère's circuital law, the induced magnetic flux density at point x is given by:

$$\begin{aligned} 2\pi(x-q)dB_{re} &= \mu_0 J_{av} t_c dq \\ 2\pi(q-x)dB_{re} &= \mu_0 J_{av} t_c dq \end{aligned} \tag{12}$$

where x is the distance between the arbitrary point and the induced eddy current.

Following Yang et al [16], the induced magnetic flux density at point x in loop 3 is obtained as:

$$B_{\mathrm{re}} = \frac{\mu_0 t_c J_{\mathrm{av}}}{2\pi} \begin{cases} \ln \dfrac{(\tau_{\mathrm{m}} - \tau_{\mathrm{i2}} - x)}{(\tau_{\mathrm{i1}} - x)}, 0 \le x < \tau_{\mathrm{i1}} \\ \ln \dfrac{(\tau_{\mathrm{m}} - \tau_{\mathrm{i2}} - x)}{(\tau_{\mathrm{m}}/2 - x)}, \tau_{\mathrm{i1}} \le x < \dfrac{\tau_{\mathrm{m}}}{2} \\ \ln \dfrac{(x - \tau_{\mathrm{i1}})}{(x - \tau_{\mathrm{m}}/2)}, \dfrac{\tau_{\mathrm{m}}}{2} \le x < \dfrac{\tau_{\mathrm{m}}}{2} + \tau_{\mathrm{c2}} \\ \ln \dfrac{(x - \tau_{\mathrm{i1}})}{(x - \tau_{\mathrm{m}} + \tau_{\mathrm{i2}})}, \dfrac{\tau_{\mathrm{m}}}{2} + \tau_{\mathrm{c2}} \le x < \tau_{\mathrm{m}} \end{cases} \tag{13}$$

The expression for the induced magnetic flux is given by:

$$\phi_{\mathrm{re}} = \int_0^{\tau_{\mathrm{p}}} B_{\mathrm{re}} w_{\mathrm{p}} dx = j\phi_{\mathrm{g}} \tag{14}$$

where in

$$\begin{aligned} \mathrm{j} = \frac{\mu_0 \sigma_{\mathrm{c}} t_{\mathrm{c}} n_2 r_{\mathrm{m}}}{60\tau_{\mathrm{m}}} \Bigg[& \int_0^{\tau_{\mathrm{i1}}} \ln \frac{(\tau_{\mathrm{m}} - \tau_{\mathrm{i2}} - x)}{(\tau_{\mathrm{i1}} - x)} dx \\ & + \int_{\tau_{\mathrm{i1}}}^{\frac{\tau_{\mathrm{m}}}{2}} \ln \frac{(\tau_{\mathrm{m}} - \tau_{\mathrm{i2}} - x)}{(\tau_{\mathrm{m}}/2 - x)} dx \\ & + \int_{\frac{\tau_{\mathrm{m}}}{2}}^{\frac{\tau_{\mathrm{m}}}{2} + \tau_{\mathrm{c2}}} \ln \frac{(x - \tau_{\mathrm{i1}})}{(x - \tau_{\mathrm{m}}/2)} dx \\ & + \int_{\frac{\tau_{\mathrm{m}}}{2} + \tau_{\mathrm{c2}}}^{\tau_{\mathrm{m}}} \ln \frac{(x - \tau_{\mathrm{i1}})}{(x - \tau_{\mathrm{m}} + \tau_{\mathrm{i2}})} dx \end{aligned} \tag{15}$$

C. Torque Calculation

Based on the equivalent magnetic circuit model shown in Figure 5 and combined with Kirchhoff's laws, the axial air gap magnetic flux in loop 3 is derived as:

$$\phi_{\mathrm{g}} = \frac{2F_{\mathrm{m}} R_{\mathrm{a}}}{(1+j)2R_{\mathrm{m}} R_{\mathrm{a}} + R_{\mathrm{l}}(2R_{\mathrm{m}} + R_{\mathrm{a}})} \tag{16}$$

Let V be the volume of the conductor disk coinciding with the permanent magnet in loop 3. The expression for the traction force is given by:

$$F_3 = \int_V |J \times B| dV = k_{\mathrm{s}} J_{\mathrm{av}} B_{\mathrm{av}} t_{\mathrm{c}} (\tau_{\mathrm{c1}} + \tau_{\mathrm{c2}}) w_{\mathrm{p}} \tag{17}$$

where k_{s} is the Russell-Norsworthy factor [24] that corrects for end effects by accounting for the current path division into the central zone (beneath magnets) and extended zone (beyond magnet edges), where the latter provides return paths for induced currents. The modified expression incorporates these geometric considerations：

$$k_{\mathrm{s}} = 1 - \frac{\tanh(\pi w_{\mathrm{p}} / 2\tau_{\mathrm{p}})}{(\pi w_{\mathrm{p}} / 2\tau_{\mathrm{p}}) \{1 + \tanh(\pi w_{\mathrm{p}} / 2\tau_{\mathrm{p}}) q_{\mathrm{c}}\}} \tag{18}$$

where q_{c} is $\tanh[\pi(r_4\text{-}r_2)/2\tau_{\mathrm{p}}]$.

The electromagnetic torque generated by the main magnetic circuit 3 is expressed as:

$$T_3 = F_3 \cdot r_{\mathrm{m}} \tag{19}$$

Similarly, the electromagnetic torque for other loops can be derived. By superposition, the total electromagnetic torque of the magnetic coupler is obtained as :

$$T = 2 \sum_{n=1}^{9} T_n \tag{20}$$

D. Transient performance during startup

The analysis of the transmission characteristics of the magnetic coupler requires consideration of the expressions for the motor torque T_M, the electromagnetic torque T_E, and the load torque T_F. Therefore, the relationship between the motor torque T_M and the input speed n_{in} is expressed as:

$$\begin{cases} T_M = \dfrac{2\lambda_{\max} T_N}{\dfrac{\beta}{\alpha} + \dfrac{\alpha}{\beta}} \\ \alpha = \lambda_{\max} + \sqrt{\lambda_{\max}^2 - 1} \\ \beta = \dfrac{n_0 - n_{\mathrm{in}}}{n_0 - n_N} \end{cases} \tag{21}$$

where n_0 is rated speed of the driving motor， n_N is the speed under rated power, n_{in} is the input speed of the motor, $\lambda_{\max}$ is the upper limit torque coefficient of the motor, and T_N is the torque under rated power of the motor.

Due to the non-contact nature of the magnetic coupler, the kinematic equations for the input and output can be expressed as:

$$\begin{cases} T_M - T_E = \dfrac{J_{in}\pi}{30} \dfrac{dn_{in}}{dt} \\ T_E - T_F = \dfrac{J_{out}\pi}{30} \dfrac{dn_{out}}{dt} \end{cases} \tag{22}$$

where J_{in} is the moment of inertia of the input $(J_{in} = 5.27 \times 10^{-2} \mathrm{kg \cdot m^2})$, J_{out} is the moment of inertia of the output $(J_{out} = 7.16 \times 10^{-2} \mathrm{kg \cdot m^2})$, and n_{in} is the input speed, and n_{out} is the output speed.

The acceleration of the permanent magnet disk and the conductor disk in the magnetic coupler is calculated as follows:

$$\begin{cases} a_{in} = \dfrac{dn_{in}}{dt} = \dfrac{30(T_M - T_E)}{J_{in}\pi} \\ a_{out} = \dfrac{dn_{out}}{dt} = \dfrac{30(T_E - T_F)}{J_{out}\pi} \end{cases} \tag{23}$$

The variation of the input speed and output speed of the magnetic coupler from time 0 to the current time t can be expressed by the following equation:

$$\begin{cases} \Delta n_{in} = \dfrac{30}{J_{in}\pi} \int_0^t (T_M - T_E) dt \\ \Delta n_{out} = \dfrac{30}{J_{out}\pi} \int_0^t (T_E - T_F) dt \end{cases} \tag{24}$$

When the magnetic coupler starts, the initial values of the input speed and output speed are 0. Therefore, the dynamic input speed n_{in} and output speed n_{out} during the startup period are given by the following equations:

$$\begin{cases} n_{in} = \Delta n_{in} \\ n_{out} = \Delta n_{out} \end{cases} \tag{25}$$

IV. Analysis of Graded Startup Characteristics of the Magnetic Coupler

A. Mechanical Characteristics Analysis

To investigate the startup torque characteristics of the slotted disk magnetic coupler, a three-dimensional simulation model is developed using finite element software. The model incorporated the parameters listed in Tables I and II. To ensure accurate simulation results and efficient computation, on-side and inside meshing were performed on each component of the coupler, based on practical conditions. The resulting finite element model mesh is shown in Figure 7.

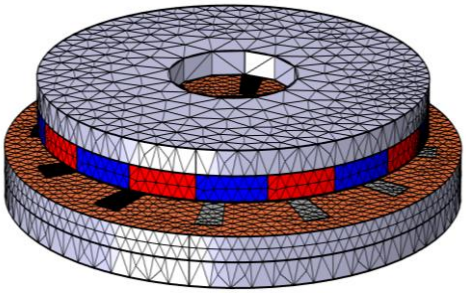

Figure 7. Mesh division model of the magnetic coupler.

Figure 8(a) shows the transient magnetic field distribution of a slotted disk magnetic coupler's conductor disk with a 6 mm air gap and a 60 rpm speed difference. The 16 uniformly distributed slots cause magnetic flux density to concentrate in the iron teeth due to their higher permeability compared to copper. The flux-focusing effect enhances the penetration of the rotating alternating magnetic field through the conductor disk, thereby improving both torque density and overall operating efficiency. As a result, the magnetic coupler achieves higher performance at the same size and power rating.

Figure 8(b) shows the induced eddy current distribution in the conductor disk under the same conditions. The speed difference between the PM rotor and the conductor rotor generates eddy currents through magnetic flux cutting. These currents form 18 elliptical loops, corresponding to the PM pole pairs. The eddy current paths circulate around the iron teeth or between adjacent teeth, determined by the arc lengths of the PMs and iron teeth, which govern the magnetic flux penetration points. This precise distribution of eddy currents not only reflects the interaction between the magnetic field and the conductor disk, but also reveals the mechanisms of energy transfer and loss in the magnetic coupler during operation.

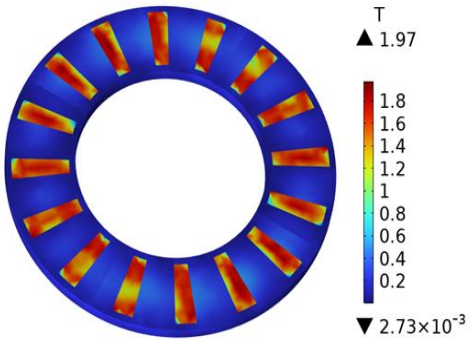

(a)Magnetic flux density (T)

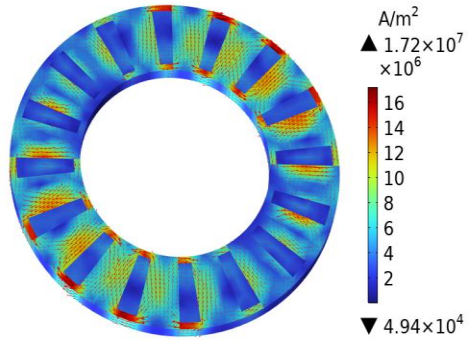

(b)Eddy current (A/m^2)

Figure 8. Magnetic field distribution.

Figure 9 illustrates the output torque variation over time for the magnetic coupler at different air gap lengths, starting at 1200 rpm under no-load conditions. The smaller the air gap thickness, the longer it takes for the magnetic coupler to reach stability. A smaller air gap leads to more complex variations in the magnetic field strength, which in turn causes the magnetic force transmission process within the coupler to take a longer time to reach equilibrium. As the air gap length gradually increases, the output torque of the magnetic coupler exhibits a distinct downward trend. This is because, with the increase in the air gap, the efficiency of magnetic field transmission is reduced, and the losses of magnetic flux lines within the air gap are increased, thereby resulting in a decrease in torque. Smaller air gap lengths result in larger torque after stable operation.

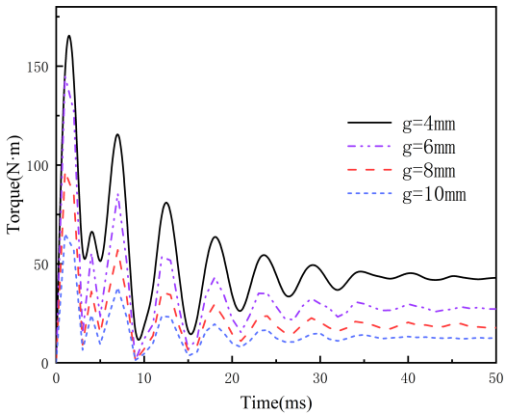

Figure 9.Torque variation curves under different air gaps.

Figures 10(a) and 10(b) show the mechanical characteristics of the magnetic coupler at different input speeds with a 4 mm air gap. With a constant air gap, the torque initially increases and then decreases as the output speed increases. This trend reflects the efficiency and stability of power transmission of the magnetic coupler under different operating conditions. At low speeds, the magnetic coupler can effectively transmit torque. However, as the speed increases, the interaction of the magnetic field and the efficiency of energy transmission may be affected to some extent, resulting in a decrease in torque.

The locked-rotor torque, which represents the output rotor's torque when the output speed is zero, is an important parameter for evaluating the starting capability of the magnetic coupler. However, it gradually decreases as the input speed increases. This suggests that the starting capability of the magnetic coupler is somewhat limited under high input speeds. This phenomenon can be attributed to the fact that high input speeds can induce excessively rapid

dynamic variations in the magnetic field, which in turn disrupt the effective coupling between the magnetic field and the rotor, ultimately leading to a reduction in the startup torque.The critical torque T_{k1} is the horizontal coordinate at the intersection of adjacent mechanical characteristic curves. At an input speed of 3400 rpm, the locked-rotor torque becomes zero, and the magnetic coupler will fail to start if the locked-rotor torque is negative.

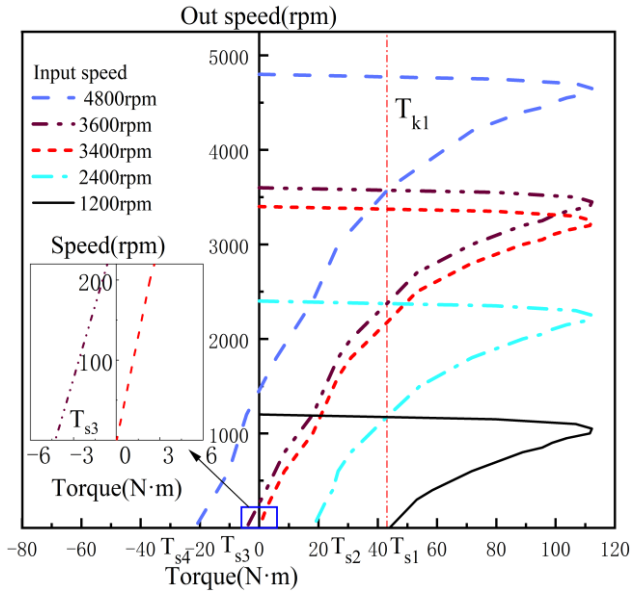

(a) Global mechanical characteristic curve

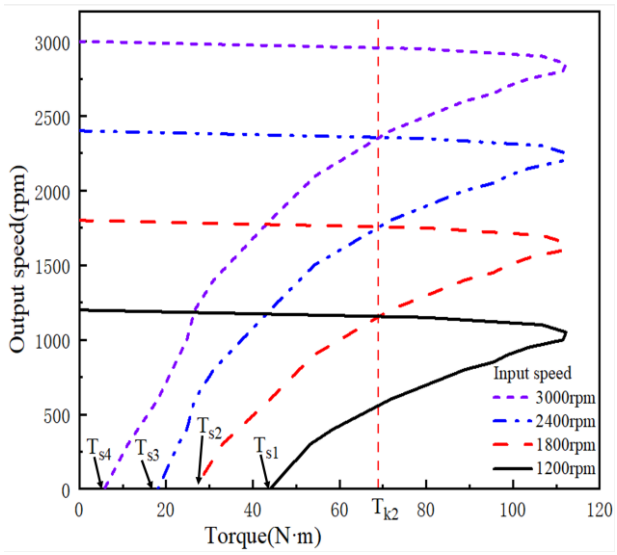

(b) Local mechanical characteristic curve

Figure 10.Mechanical characteristic curves under different input speeds.

B. Simulation Analysis of Graded Soft-Start Characteristics

To address startup challenges with high-speed differences and heavy loads, a graded approach gradually increases the input speed to the magnetic coupler. As input speed rises, the locked-rotor torque decreases, reducing the output rotor's angular acceleration. To counteract the difficulty in starting at higher rated input speeds (where locked-rotor torque is lower), a resistor box is connected in series with the input motor's rotor circuit. This resistor box adjusts resistance during operation: the resistance is constant; after connection, it increases, reducing the starting current.

As shown in Figure 11, the synchronous speed (n) and maximum output torque (T_m) remain constant throughout the starting process, indicating that the steady-state performance of the system is not affected by the graded starting strategy. This result confirms the effectiveness of the graded starting strategy, which optimizes the starting process without compromising the normal operating performance of the system. However, the critical output speed (n_m) is inversely proportional to the rotor circuit's total resistance. Increasing the resistance lowers the output speed, thereby improving the starting torque.

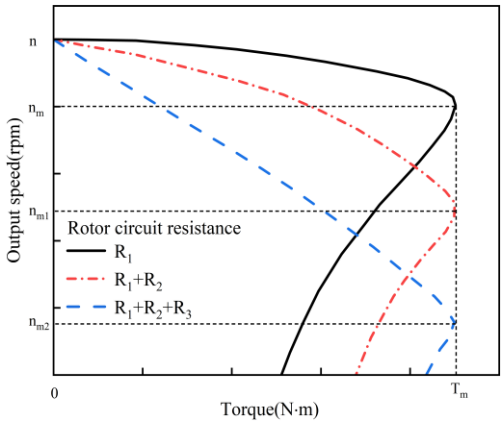

Figure 11. Mechanical characteristic curves with different rotor circuit resistances

A graded approach to controlling the PM disk speed accelerates the conductor disk's transition from stationary to stable rotation. This method maintains sufficient locked-rotor torque at each stage by gradually increasing the magnetic coupler's input speed, ensuring normal system startup.

Directly setting the input speed to 4800 rpm under no-load conditions resulted in startup failure due to insufficient locked-rotor torque. Instead, the PM disk was initiated at 1200 rpm (Figure 12). After 245 ms, the speed was increased to 2400 rpm, and this process was repeated until the magnetic coupler stabilized at 4800 rpm. This graded speed control significantly reduces the time required for the conductor disk to achieve stable operation at 4800 rpm.

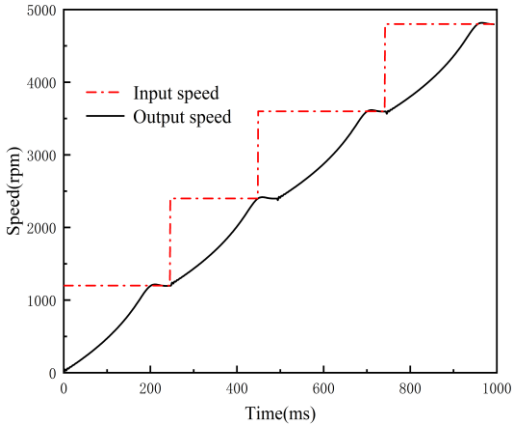

Figure 12. No-load graded start-up speed/time and torque/time response curves

Applying a load to the magnetic coupler's output requires the locked-rotor torque to exceed both a minimum value and the load torque itself for successful startup. As shown in Figure 9(b), the critical load torque (T_{k2}) at the intersection of adjacent mechanical characteristic curves under different input speeds is 68.96 N·m. With a 30 N·m load and an input speed of 1200 rpm, the locked-rotor torque

(T_{s1}) is 43.96 N·m, exceeding the load torque and enabling startup. However, at 1800 rpm, the locked-rotor torque (T_{k2}) is 28.36 N·m, which is less than the load torque, preventing startup. Therefore, a graded soft-start strategy is implemented for the magnetic coupler to address this issue.

Figure 13(a) illustrates the magnetic coupler's output speed response over time, with a 4 mm air gap, an input speed range of 0–3000 rpm, and a 30 N·m load torque. Normal startup occurs when the critical load torque exceeds the locked-rotor torque, but remains below the first-level locked-rotor torque of 50.6 N·m. The output speed initially fluctuates due to the pre-startup total magnetic field, then dynamically stabilizes around 40 ms due to the induced magnetic field, reaching a maximum of 1181 rpm at approximately 450 ms. During the transition to the second-level startup speed of 1800 rpm, the input speed briefly fluctuates to rebalance the air gap magnetic field before quickly stabilizing. The output speed then stabilizes at 1776 rpm, maintaining a speed difference below 30 rpm in subsequent levels. The first-level startup time is longer due to the larger initial speed difference.

As illustrated in Figure 13(b), fluctuations in the air gap's magnetic field during the magnetic coupler's startup lead to variations in input torque. At each stage of the graded startup, the input torque remains higher than the load torque, causing angular acceleration. As the input speed increases, the input torque peaks before decreasing to match the load torque. Consequently, this graded startup approach is essential for efficiently accelerating magnetic couplers with substantial loads to their operational speed.

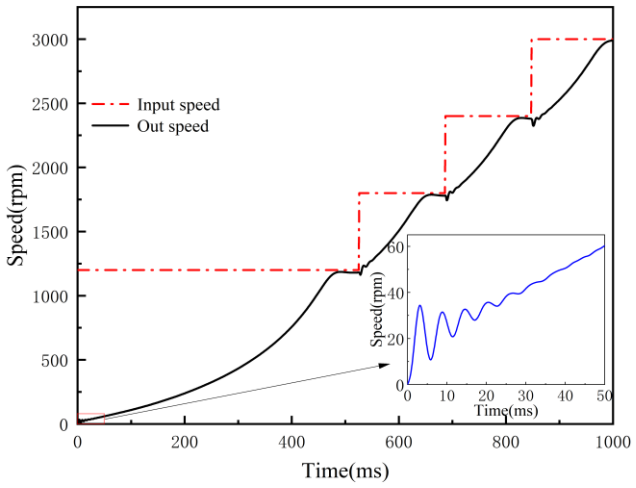

(a)Speed-time response curve

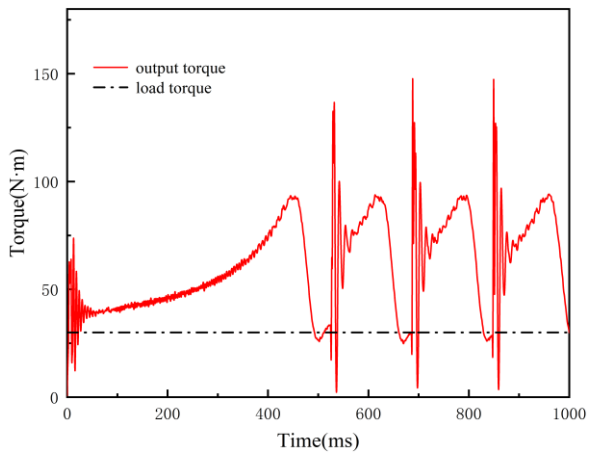

(b) Torque-time response curve

Figure 13. Speed/torque-time response curve of 30 N·m load

V. Experimental Verification

A. Experimental Platform Setup

As shown in Figure 14, a torque-speed experimental platform was specifically constructed to verify the theoretical calculations and torque performance of the slotted disk magnetic coupler. The platform features a drive motor that powers the permanent magnet PM disk to ensure its normal operation. High-precision torque sensors are installed to measure and record the input and output torque as well as speed data in real time, providing accurate and reliable data support for the experiment. Additionally, a load motor is connected to the conductor disk to simulate actual working conditions by providing variable loading conditions for the magnetic coupler.

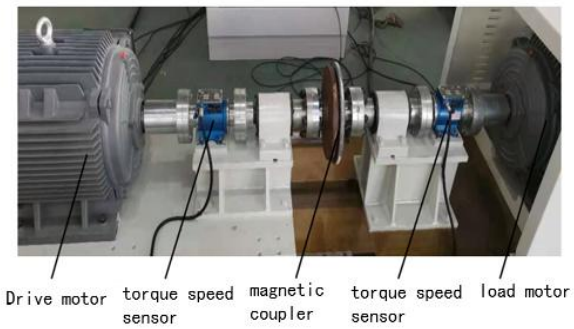

Figure 14. Experimental measurement platform.

B. Experimental Results and Analysis

The theoretical output torque values, calculated for a 4 mm air gap across varying speed differences, demonstrate a strong correlation with both finite element simulation and experimental results. During the graded startup process, the speed difference is carefully maintained below 30 rpm, ensuring smooth acceleration. In Figure 15, the dynamic behavior of the system can be characterized by three distinct operational zones. First, in the no-load zone, the output speed rapidly accelerates to its rated value, with the electromagnetic torque peaking initially before diminishing to zero upon synchronization. Second, in the loading zone, an increased load extends the stabilization period. Here, the steady-state electromagnetic torque balances the load torque, resulting in a proportional reduction in the output speed. Finally, in the slip zone, when the load exceeds the maximum transmissible capacity of the coupler, both the electromagnetic torque and the output speed experience a decline.

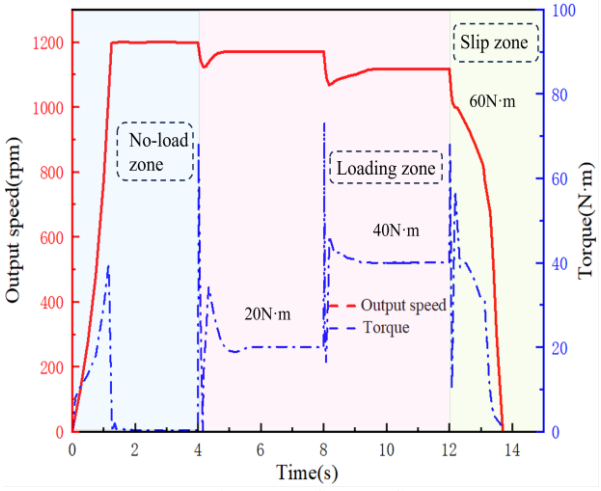

Fig. 15. Loading test diagram

As shown in Figure 16, output torque values closely align when the speed difference is below 80 rpm. Beyond this, experimental values are lower than theoretical and simulation results. The discrepancy is primarily attributed to two factors: demagnetization of permanent magnets during long-term storage, which reduces magnetic field strength and torque output, and frictional losses in the experimental platform that diminish torque transmission efficiency.

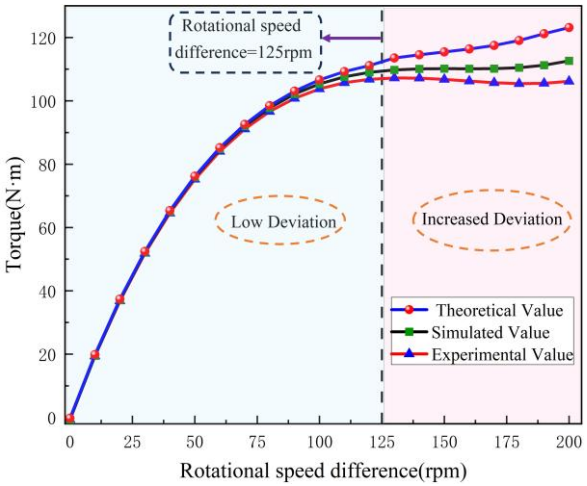

Figure 16. Output torque variation curve with speed difference.

VI. Conclusions

This research systematically addresses the startup limitations of slotted disc-type magnetic couplers operating under high-speed slip and heavy-load conditions. A validated equivalent magnetic circuit (EMC) model is presented, enabling the design of a graded soft-start strategy. The EMC model's accuracy is confirmed through finite element analysis and experimental validation, demonstrating its capability to predict the magnetic coupler characteristics during startup. Moreover, the proposed soft-start strategy effectively mitigates startup failures caused by insufficient locked-rotor torque, thereby ensuring reliable and stable operation. Consequently, this study provides a scientific basis for the design and development of magnetic couplers intended for high-speed slip and heavy-load conditions.

References

[1] V. Aberoomand, M. Mirsalim, and R. Fesharakifard, "Design optimization of double-sided permanent-magnet axial eddy-current couplers for use in dynamic applications," IEEE Transactions on Energy Conversion, vol. 34, no. 2, pp. 909-920, 2018.

[2] L. Aman, J. Abbott, and S. Roundy, "Optimal parametric design of radial magnetic torque couplers via dimensional analysis," IEEE Transactions on Magnetics, vol. 58, no. 6, pp. 1-8, 2022.

[3] B. Liu, T. Zhang, H. Zhang, Z. Zhang, and Y. Cao, "Simulation analysis on electromagnetic vibration and noise of novel mechatronic-electro-hydraulic coupler," Machines, vol. 10, no. 9, pp. 762, 2022.

[4] Y. Qi, C. Yang, Y. Zhang, C. Guo, and A. W. Tadesse, "Torque Characteristics Analysis of Slotted-Type Axial-Flux Magnetic Coupler in the Misalignment State," Machines, vol. 12, no. 11, pp. 751, 2024.

[5] J. Wang, H. Lin, S. Fang, and Y. Huang, "A general analytical model of permanent magnet eddy current couplings," IEEE Transactions on Magnetics, vol. 50, no. 1, pp. 1-9, 2013.

[6] X. Yang, Y. Liu, and L. Wang, "An improved analytical model of permanent magnet eddy current magnetic coupler based on electromagnetic-thermal coupling," IEEE Access, vol. 8, pp. 95235-95250, 2020.

[7] A. Barmpatza and J. Kappatou, "Investigation of the combined eccentricity and demagnetization fault in an AFPMSG," in 2020 International Conference on Electrical Machines (ICEM), 2020, vol. 1: IEEE, pp. 1377-1383.

[8] Y. Chaojun, A. Wondimu Tadesse, F. Yang, G. Lixiang, and W. Ao, "Torque and eddy current behavior of a magnet rotating axial disk type magnetic coupler: analysis and experimental verification," IETE Journal of Research, vol. 70, no. 12, pp. 8580-8591, 2024.

[9] A. S. Erasmus and M. J. Kamper, "Computationally efficient analysis of double PM-rotor radial-flux eddy current couplers," IEEE Transactions on industry applications, vol. 53, no. 4, pp. 3519-3527, 2017.

[10] T. Lubin and A. Rezzoug, "Improved 3-D analytical model for axial-flux eddy-current couplings with curvature effects," IEEE Transactions on Magnetics, vol. 53, no. 9, pp. 1-9, 2017.

[11] J. Wang, "A generic 3-D analytical model of permanent magnet eddy-current couplings using a magnetic vector potential formulation," IEEE Transactions on industrial electronics, vol. 69, no. 1, pp. 663-672, 2021.

[12] C. Yang, S. Zheng, Z. Peng, J. Zhu, and Y. Ding, "A steady-state and dynamic response model for working characteristics prediction of the electromechanical transmission system including eddy-current magnetic coupler," International journal of applied electromagnetics and mechanics, no. Preprint, pp. 1-22, 2024.

[13] K. Deshan, W. Dazhi, L. Wenhui, W. Sihan, and H. Zhong, "Analysis of a novel flux adjustable axial flux permanent magnet eddy current coupler," IET Electric Power Applications, vol. 17, no. 2, pp. 181-194, 2023.

[14] B. Guo, D. Li, J. Shi, and Z. Gao, "A performance prediction model for permanent magnet eddy-current couplings based on the air-gap magnetic field distribution," IEEE Transactions on Magnetics, vol. 58, no. 5, pp. 1-9, 2022.

[15] C. Xikang, L. Wei, Z. Yang, L. Sitong, and L. Weiqi, "A concise transmitted torque calculation method for pre-design of axial permanent magnetic coupler," IEEE Transactions on Energy Conversion, vol. 35, no. 2, pp. 938-947, 2020.

[16] C. Yang, Z. Peng, J. Tai, L. Zhu, B. J. K. Telezing, and P. D. Ombolo, "Torque characteristics analysis of slotted-type eddy-current couplings using a new magnetic equivalent circuit model," IEEE Transactions on magnetics, vol. 56, no. 9, pp. 1-8, 2020.

[17] F. Yang, J. Zhu, C. Yang, Y. Ding, and T. Hang, "A simple method to calculate the torque of magnet-rotating-type axial magnetic coupler using a new magnetic equivalent circuit model," IEEE Transactions on magnetics, vol. 58, no. 11, pp. 1-12, 2022.

[18] S. Alshammari, P. Lazari, and K. Atallah, "Comparison of eddy current coupling topologies for high efficiency mechanical power transmission," IEEE Transactions on energy conversion, vol. 38, no. 2, pp. 982-992, 2022.

[19] Y. Chaojun, W. Yingzhi, L. Kang, L. Zhibao, Z. Weifeng, and L. Ming, "Analysis for axial force of slotted-type axial-flux magnetic coupler," in 2017 5th International conference on mechanical, automotive and materials engineering (CMAME), 2017: IEEE, pp. 359-364.

[20] X. Dai, Q. Liang, J. Cao, Y. Long, J. Mo, and S. Wang, "Analytical modeling of axial-flux permanent magnet eddy current couplings with a slotted conductor topology," IEEE Transactions on Magnetics, vol. 52, no. 2, pp. 1-15, 2015.

[21] D. Kong, D. Wang, Y. Ni, K. Song, Y. Qi, and Y. Li, "Analytical Analysis of a Novel Flux Adjustable Permanent Magnet Eddy Current Coupling with Double-Sided Conductor," in Actuators, 2023, vol. 12, no. 3: MDPI, pp. 105.

[22] T. Lubin and A. Rezzoug, "3-D analytical model for axial-flux eddy-current couplings and brakes under steady-state conditions," IEEE Transactions on magnetics, vol. 51, no. 10, pp. 1-12, 2015.

[23] J. Wang and J. Zhu, "A simple method for performance prediction of permanent magnet eddy current couplings using a new magnetic equivalent circuit model," IEEE Transactions on industrial electronics, vol. 65, no. 3, pp. 2487-2495, 2017.

[24] R. Russell and K. Norsworthy, "Eddy currents and wall losses in screened-rotor induction motors," Proceedings of the IEE-Part A: Power engineering, vol. 105, no. 20, pp. 163-175, 1958.

Chaojun Yang is currently a Professor and Ph.D. Supervisor at the School of Mechanical Engineering, Jiangsu University, Zhenjiang, China. Her research focuses on permanent magnet transmission and laser processing technologies, with over 200 peer-reviewed papers published in these fields.

Yuan Gao received the B.S. degree in Mechatronics Engineering from Shandong University, Jinan, China. He is currently pursuing the M.S. degree at Jiangsu University, Zhenjiang, China. His research focuses on permanent magnet transmission.

Jian Wang received his B.Eng. in Mechanical Engineering from Lanzhou University of Technology, Lanzhou, China. He has obtained his M.S. degree at Jiangsu University, Zhenjiang, China. His research focuses on permanent magnet transmission.